Static and dynamic characteristics of integrated semiconductor optical parametric oscillators

Nima Zareian and Amr S. Helmy*

Edward S. Rogers Sr. Department of Electrical and Computer Engineering, University of Toronto, 10 King's College Rd., Toronto, Ontario ON M5S 3G4, Canada
**Corresponding author: a.helmy@utoronto.ca*

Received May 6, 2013; revised July 3, 2013; accepted July 4, 2013;
posted July 8, 2013 (Doc. ID 189007); published July 31, 2013

The static and dynamic properties of semiconductor optical parametric oscillators (SOPOs) are studied by merging the rate equations of the diode pump laser with those of the OPO while taking into account the phase and, hence, chirp performance. The static analysis of the SOPO shows two stable regimes of operation, namely, an efficient and an inefficient regime akin to the case for conventional intracavity OPO. The large signal dynamic properties of the SOPO are studied in the two static operating regimes. The study shows that there exists enormous negative and positive frequency chirp in the signal and idler in the order of a few terahertz upon large signal modulation. These characteristics are explained through the well-known properties of the nonlinear gain medium of the OPO. The limitations on using these devices in a directly modulated fashion are discussed. Such limitations are found to be determined largely by the SOPO rise time in certain bias conditions.

OCIS codes: (140.2020) Diode lasers; (190.4390) Nonlinear optics, integrated optics; (130.7405) Wavelength conversion devices; (190.4975) Parametric processes.
http://dx.doi.org/10.1364/JOSAB.30.002306

1. INTRODUCTION

Due to their vastly tunable output properties and versatility, optical parametric oscillators (OPOs) have fueled many domains of applications, such as spectroscopy [1,2], sensing [3,4], and various quantum optical experiments [5,6]. In particular, tabletop intracavity optical parametric oscillators (IOPOs) have been investigated since the late 1960s using various nonlinear elements in doubly resonant [7,8] and singly resonant configurations [9–11]. IOPOs offer distinct advantages over other OPO configurations, especially due to the lower threshold pump power needed in the CW mode of operation. In the case of IOPOs, parametric generation takes place in the same cavity where the lasing takes place. This leads to a larger pump power available inside the laser cavity and, consequently, to lower threshold levels compared with conventional OPOs. A notable limitation of these systems is instability due to relaxation oscillations [12]. Operating the pump laser in the Q-switched pulsed mode is one of the solutions to overcome this stability issue [10,11].

While all IOPOs reported to date utilize bulk optical elements or fibers, recent developments in the field of integrated photonics usher in a new era of integrated electrically injected semiconductor optical parametric oscillators (SOPOs) [13,14]. These devices can provide numerous advantages due to their robustness, low power consumption, compact form factor, and being alignment free. Recently, a platform conducive to realizing SOPOs has been developed, namely active Bragg reflection waveguides [15,16]. Self-pumped electrically injected SOPOs can be implemented through designing edge emitting semiconductor Bragg reflection waveguide lasers (BRLs), which have their second-order nonlinearities phase matched for efficient parametric conversion between the pump, signal, and idler. The coherent radiation obtained from BRLs will provide the pump power, which will be down converted into a signal and idler. Through this approach, self-pumped parametric fluorescence was reported in GaAs/AlGaAs BRLs [17]. This is the essential stepping stone needed for an SOPO as self-pumped parametric fluorescence is the output of an SOPO operating below oscillation threshold. When sufficient parametric gain is made available to the parametric process, both signal and idler can reach oscillation threshold in the same cavity as the laser pump. The resulting devices have properties that are similar in part to the characteristics of both diode lasers and OPOs.

Akin to the optimization of the IOPO cavity that took place prior to the realization of efficient IOPOs, similar quantitative design tools and insight are needed for enabling the realization of functional SOPOs. Some SOPO design trade-offs, including the OPO threshold power, have been studied recently [18]. This recent study focused on time-invariant properties, where the static operating regimes and dynamics of power exchange in the SOPO were left unexamined. Understanding the dynamic and static properties of SOPOs is essential to their optimal design and applicability to certain domains, especially in the pulsed regime. Insight into the device dynamics requires concomitant large signal analysis of the rate equations of both the pump part and the OPO part of the device. As such, in this article we will utilize existing rate equations of both diode lasers and OPOs and modify them in order to represent the operation of SOPOs. This will help to shed light on the device physics of operation and elucidate its static and dynamic properties. Some similar models have been used previously for static and dynamic analysis of tabletop intracavity doubly resonant [7,8,19] and singly resonant [9,10] OPOs. Although doubly resonant OPOs allow for lower

threshold powers, often singly resonant OPOs are favored due to their superior stability properties and fewer resonance constraints. In this article, we have focused on a doubly resonant SOPO to facilitate OPO threshold powers low enough to be achievable by the performance of readily available integrated devices.

In addition to developing the rate equations to predict and optimize the performance of the presented integrated OPOs, this study is distinct from previous reports in various aspects: the equations describing the pump lasers implemented here are those for a semiconductor diode laser cavity instead of those describing solid state lasers; the nonlinear interactions are reformulated for waveguides rather than bulk crystals; and more importantly, an explicit account for the phase of the interacting fields is introduced in the equations used here allowing for chirp analysis of SOPOs.

Changes in the laser frequency due to carrier density induced refractive index change, namely chirp, is a well-studied by-product of direct modulation in semiconductor diode lasers. Direct modulation of semiconductor lasers is an attractive solution for amplitude shift keying (ASK) optical communication systems. Semiconductor laser chirp becomes important in dispersion-limited systems such as long-haul or medium-haul telecommunication networks operating at 1550 nm, and therefore, there have been numerous studies on chirp engineering to mitigate such issues in telecommunication systems [20,21]. Similar to semiconductor diode lasers, SOPOs can be directly modulated and would exhibit frequency chirp not only in the pump but also in signal and idler wavelengths. As such, frequency chirp is expected to have significant impact on the operating characteristics of SOPOs; hence, chirp effects are included in the present SOPO model and will be investigated in the article.

This article is organized as follows. Section 2 outlines the derivation of the SOPO rate equations. The developed model combines the diode laser rate equations and OPO rate equations to allow for investigating the time evolution of population inversion as well as pump, signal, and idler phases and powers within the SOPO cavity. Initially these equations are investigated to identify the SOPO steady-state regimes in Section 3. The time evolution properties of the SOPO are then studied in detail through solving the equations numerically using a Runge–Kutta technique in Section 4. These solutions are then used to analyze and explain the time-dependent performance of SOPOs in each regime in the rest of Section 4. This study unfolds some unique modulation and chirp properties of SOPOs, which can be of great benefit for various applications such as directly current modulated devices for optical communications. To provide further insight into the SOPO dynamics, an analytical approximation is derived in the same section for the rise time of the parametric processes and is compared to the numerical solutions. A discussion of the performance observed in this class of SOPOs is then provided in Section 5. Finally, a conclusion is provided in Section 6.

2. FORMALISM: RATE EQUATIONS IN ACTIVE, NONLINEAR MEDIA

The classical rate equations of quantum well (QW) lasers are well studied in the literature. The power and phase rate equations can be derived by solving the Helmholtz electric field equation, assuming slowly a varying envelope, multiplying by the field envelopes in x, y, and z, and integrating over all three directions. The laser rate equations can be expressed as follows [22] for the carrier density N, average laser optical power inside the cavity P_p, and radiation phase ϕ_p:

$$\frac{dP_p}{dt} = P_p v_{g;p}\left(\Gamma \frac{g}{1+\beta P_p} - \alpha_p\right), \tag{1a}$$

$$\frac{d\phi_p}{dt} = -\frac{\alpha}{2} v_{g;p}(\Gamma g - \alpha_p), \tag{1b}$$

$$\frac{dN}{dt} = \frac{\eta I}{qV} - \frac{N}{\tau} - \frac{g v_{g;p} \zeta P_p}{1+\beta P_p}, \tag{1c}$$

$$\zeta = \frac{L}{\hbar \omega_p V_{\mathrm{ph}} v_{g;p}}. \tag{1d}$$

Here Γ is the optical confinement factor, g is the optical gain, β represents gain saturation, $v_{g;p}$ is the group velocity at the laser wavelength, α_p represents the sum of distributed mirror loss and propagation losses, α is the linewidth enhancement factor, η denotes the current injection efficiency, I is the injected current, q represents the electron charge, V is the active layer volume, V_{ph} is the optical cavity volume, τ is the carrier lifetime, ζ is a conversion factor between the internal power and photon density in the cavity, L is the length of the cavity, ω_p is the angular frequency of the laser, and $\hbar$ denotes the Dirac constant. In these equations, the spontaneous emission factor is neglected. Note that the rate equations are given for the laser internal power so as to facilitate combining them with those of the OPO later in the text. Also note that while the confinement factor Γ shows up in Eq. (1a), this factor is excluded from Eq. (1c) due to the use of carrier density rather than carrier numbers in this equation [23].

If the diode laser cavity is phase matched for second-order nonlinearities, efficient optical parametric processes can take place within that cavity. A schematic of the device is illustrated in Fig. 1, where pump photons are generated through lasing action in the active medium and the pair of signal and idler are generated by parametric downconversion of these high energy pump photons. As such, a part of the laser power is converted into signal and idler where their wavelengths are governed by the phase-matching condition. This downconversion translates into an extra source of loss for the pump laser.

Assuming a single longitudinal mode for all three interacting waves in the SOPO and taking z as the propagation direction, the overall scalar electric field can be expressed as

$$E_\sigma(x,y,z,t) = \frac{1}{2} F_\sigma(x,y) f_\sigma(z) \mathcal{E}_\sigma(t) \exp[-i\omega_\sigma t + i\phi_\sigma(t)] + \text{c.c.},$$
$$\sigma \in \{p,s,i\}. \tag{2}$$

In Eq. (2), pump, signal, and idler are represented by subscripts p, s, and i, respectively; $\mathcal{E}_\sigma(t)$ are the absolute values of the time envelopes; F_σ are the normalized field profiles in the transverse plane (xy-plane); f_σ are the field envelopes along the propagation direction; and c.c. denotes complex conjugate. Similar to the work of Oshman and Harris in [7],

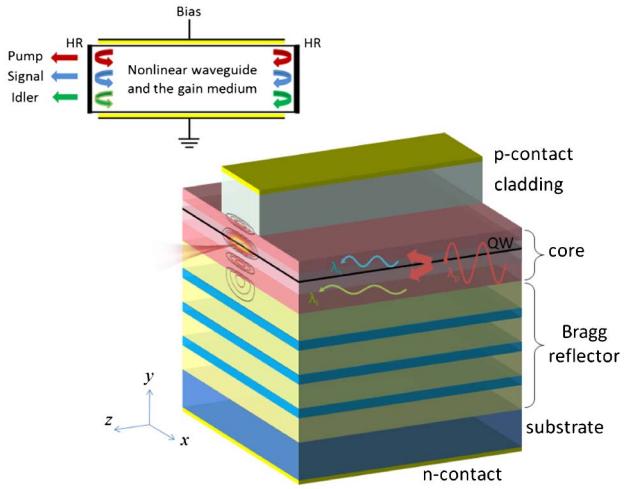

Fig. 1. Schematic of a representative doubly resonant SOPO where the end facets of the diode laser are high reflection coated (HR) at pump, signal, and idler wavelengths. A scheme of a typical Bragg reflection waveguide SOPO is shown.

the z envelopes are set to $f_p(z) = \sqrt{2/L}\cos(k_p z)$, $f_s(z) = \sqrt{2/L}\sin(k_s z)$, and $f_i(z) = \sqrt{2/L}\sin(k_i z)$, where k_σ are the propagation constants at laser threshold. The laser acts as the pump, where $\omega_p = \omega_s + \omega_i$. The internal powers of the pump, signal, and idler are normalized such that $P_\sigma = cn_\sigma\epsilon_0/2L\mathcal{E}_\sigma^2$ where n_σ are the real parts of the corresponding effective refractive indices, and c and ϵ_0 are the speed of light and permittivity in vacuum. Note that many diode laser designs operate in a single longitudinal mode. As SOPOs are essentially diode lasers with the nonlinearity phase matched, the single mode assumption can be valid for SOPOs as well.

By substituting Eq. (2) into the Helmholtz equation, a set of nonlinear rate equations for SOPOs can be derived similar to the derivation of the diode laser rate equation. Under slowly varying amplitude approximation, by multiplying both sides of the Helmholtz equations by F_σ and f_σ and integrating over x, y, and z, the rate equations for the powers of the interacting waves can be derived as

$$\frac{dP_p}{dt} = P_p v_{g;p}\left(\Gamma\frac{g}{1+\beta P_p} - \alpha_p\right) + Kv_{g;p}\frac{\kappa}{\lambda_p}\sqrt{P_s P_i P_p}(-\sin(\Delta\phi))\mathrm{sinc}(\Delta kL), \tag{3a}$$

$$\frac{d\phi_p}{dt} = -\Delta\omega_p + \frac{K}{2}v_{g;p}\frac{\kappa}{\lambda_p}\sqrt{\frac{P_s P_i}{P_p}}\cos(\Delta\phi)\mathrm{sinc}(\Delta kL), \tag{3b}$$

$$\frac{dP_s}{dt} = -P_s v_{g;s}\alpha_s + Kv_{g;s}\frac{\kappa}{\lambda_s}\sqrt{P_s P_i P_p}\sin(\Delta\phi)\mathrm{sinc}(\Delta kL), \tag{3c}$$

$$\frac{d\phi_s}{dt} = -\Delta\omega_s + \frac{K}{2}v_{g;s}\frac{\kappa}{\lambda_s}\sqrt{\frac{P_p P_i}{P_s}}\cos(\Delta\phi)\mathrm{sinc}(\Delta kL), \tag{3d}$$

$$\frac{dP_i}{dt} = -P_i v_{g;i}\alpha_i + Kv_{g;i}\frac{\kappa}{\lambda_i}\sqrt{P_s P_i P_p}\sin(\Delta\phi)\mathrm{sinc}(\Delta kL), \tag{3e}$$

$$\frac{d\phi_i}{dt} = -\Delta\omega_i + \frac{K}{2}v_{g;i}\frac{\kappa}{\lambda_i}\sqrt{\frac{P_p P_s}{P_i}}\cos(\Delta\phi)\mathrm{sinc}(\Delta kL). \tag{3f}$$

These equations can be coupled with the carrier density rate Eq. (1c) to describe the interaction of carriers and photons for all three waves. In Eq. (3), α_σ represent the sum of propagation loss and distributed mirror losses for each wavelength, λ_σ are the free space wavelengths, $K = 1/2$ for the degenerate three-wave mixing process, and $K = 1$ for the nondegenerate case, $\Delta\phi = \phi_p - \phi_s - \phi_i$, $\Delta k = k_p - k_s - k_i$, and κ is the nonlinear coupling coefficient and is given by

$$\kappa = \sqrt{\frac{\langle\chi_{\mathrm{eff}}^{(2)}\rangle^2 4\pi^2}{n_s n_i n_p \epsilon_0 c A_{\mathrm{eff}}^{(2)}}}, \tag{4a}$$

$$\langle\chi_{\mathrm{eff}}^{(2)}\rangle = \frac{\iint_{-\infty}^{+\infty} F_s(x,y)F_i(x,y)F_p(x,y)\chi_{\mathrm{eff}}^{(2)}(x,y)\mathrm{d}x\mathrm{d}y}{\int_{-\infty}^{+\infty} F_s(x,y)F_i(x,y)F_p(x,y)\mathrm{d}x\mathrm{d}y}, \tag{4b}$$

$$A_{\mathrm{eff}}^{(2)} = \frac{\iint_{-\infty}^{+\infty} F_s^2(x,y)\mathrm{d}x\mathrm{d}y \iint_{-\infty}^{+\infty} F_i^2(x,y)\mathrm{d}x\mathrm{d}y \iint_{-\infty}^{+\infty} F_p^2(x,y)\mathrm{d}x\mathrm{d}y}{\left(\iint_{-\infty}^{+\infty} F_s(x,y)F_i(x,y)F_p(x,y)\mathrm{d}x\mathrm{d}y\right)^2}. \tag{4c}$$

Here $\chi_{\mathrm{eff}}^{(2)}(x,y)$ is the local effective second-order susceptibility of the material, and $\langle\chi_{\mathrm{eff}}^{(2)}\rangle$ is the effective susceptibility of the device—a weighted average of the susceptibility where the field profiles are the weighting functions. Additionally, in Eqs. (3d) and (3f), $\Delta\omega_{s,i}$ are the deviations of signal and idler frequencies from their values at laser threshold due to laser frequency chirp $\Delta\omega_p$. As shown in the Appendix, for a small change in the pump frequency, $\Delta\omega_p = (\alpha/2)v_{g;p}(\Gamma g - \alpha_p)$, the associated changes in the signal and idler frequencies can be derived from the energy and momentum conservation relations as

$$\Delta\omega_p = \frac{\alpha}{2}v_{g;p}(\Gamma g - \alpha_p), \tag{5a}$$

$$\Delta\omega_s = \Delta\omega_p\frac{n_p - n_{g;i} - n_{g;p}}{n_{g;s} - n_{g;i}} = \gamma\Delta\omega_p, \tag{5b}$$

$$\Delta\omega_i = \Delta\omega_p - \Delta\omega_s, \tag{5c}$$

where n_σ are the real parts of the corresponding effective indices and $n_{g;\sigma}$ represent the group index at each wavelength.

In contrast to bulk IOPOs where frequency chirp of the pump is not usually of great significance as the pump is either CW or Q-switched, SOPOs can be operated in pulsed mode similar to a directly modulated laser diode. Operating in this mode entails appreciable pump frequency chirp. This chirp of the pump can play a major role in shaping the output properties of the signal and the idler. Therefore, the terms $\Delta\omega_p$, $\Delta\omega_s$, and $\Delta\omega_i$ which are dependent on the injection current have to

be taken into account in the study of the SOPO chirp and power characteristics.

3. STEADY-STATE ANALYSIS

The model derived here for doubly resonant SOPOs is similar in form to the doubly resonant IOPO model discussed by Oshman and Harris [7], despite the differences between both devices. In the case of the SOPO, waves propagate in guided modes in a cavity with relatively smaller dimensions, which can support a smaller number of longitudinal modes in comparison to a conventional IOPO cavity. Another difference in the mathematical expression of the two sets of equations is the manifestation of frequency chirp $\Delta\omega_p$ in the pump frequency and the corresponding signal and idler chirp as described in Eq. (5). As shown in the Appendix, the effect of frequency chirp can be accounted for in a first-order approximation by utilizing the energy conservation condition, where the chirp terms cancel out in $d\Delta\phi/dt$. As such, when calculating the SOPO characteristics that deal with $\Delta\phi$ rather than individual phases of the interacting waves, the chirp effects will not play a significant role. This is indeed the case when examining the SOPO steady-state regimes, which relate closely to those of doubly resonant IOPOs as will be shown in this section.

A. Stability Conditions

The SOPO steady-state pump, signal, and idler internal cavity powers can be derived using Eq. (3). Similar to the approach taken in doubly resonant IOPOs, by setting the time derivatives of carrier density, powers and $\Delta\phi$ to zero, three distinct solutions can be found for the SOPO output, defining three regions of operation.

It can be shown that if the pump laser power is below the OPO threshold power $P_{\mathrm{OPO,th}}$, which is described by

$$P_{\mathrm{OPO,th}} = \frac{1}{4}\frac{\lambda_i\lambda_s\alpha_i\alpha_s}{\kappa^2}, \tag{6}$$

parametric oscillation will not take place and the laser will operate similar to a conventional semiconductor laser that is not phase matched. This regime will be termed as the no OPO regime since there will be no power available for either the signal or idler. The pump power in this regime is described by

$$P_{p,\text{no-OPO}} = \frac{\Gamma g v_g \tau_p - 1}{\beta}. \tag{7}$$

If the value of $P_{p,\text{no-OPO}}$ is above $P_{\mathrm{OPO,th}}$, there are two possible steady-state operating regimes depending on the value of $\Delta\phi$. In the inefficient regime of operation $\Delta\phi \neq (\pi/2)$. In this case, $\Delta\phi$ can take on any arbitrary number and the parametric interaction changes the waves' phases in addition to their amplitudes. Beside the SOPO threshold condition, for the inefficient regime to be in effect it is necessary that $P_{p,\mathrm{ineff}} > 0$ and $\sin(\Delta\phi_{\mathrm{ineff}}) \leq |1|$ where the powers and $\Delta\phi_{\mathrm{ineff}}$ in this regime are defined as

$$P_{p,\mathrm{ineff}} = \frac{g\Gamma v_{g;p} - \alpha_i v_{g;i} - \alpha_p v_{g;p} - \alpha_s v_{g;s}}{\beta(\alpha_s v_{g;s} + \alpha_p v_{g;p} + \alpha_i v_{g;i})}, \tag{8a}$$

$$P_{s,\mathrm{ineff}} = P_{p,\mathrm{ineff}}\frac{\lambda_p(v_{g;s}\alpha_s + v_{g;i}\alpha_i)}{\lambda_s\alpha_s v_{g;s}}, \tag{8b}$$

$$P_{i,\mathrm{ineff}} = P_{p,\mathrm{ineff}}\frac{\lambda_p(\alpha_s v_{g;s} + \alpha_i v_{g;i})}{\lambda_i\alpha_i v_{g;i}}, \tag{8c}$$

$$\sin^2(\Delta\phi_{\mathrm{ineff}}) = \frac{P_{\mathrm{OPO,th}}}{P_{p;\mathrm{ineff}}}. \tag{8d}$$

Note that an "ineff" subscript is added to the power and phase expressions above to clearly represent the inefficient regime of operation.

On the other hand, in the efficient regime, $\Delta\phi = \pi/2$ that leads to zero nonlinear terms in Eqs. (3b), (3d), and (3f). For this regime to be valid, the SOPO should be operating above threshold, and the inefficient regime should be unstable; the second condition implies that either $P_{p,\mathrm{ineff}} < 0$ or $\sin(\Delta\phi_{\mathrm{ineff}}) > |1|$ should be valid. The pump, signal, and idler powers are defined as the following in the efficient regime:

$$P_{p,\mathrm{eff}} = P_{\mathrm{OPO,th}}, \tag{9a}$$

$$P_{s,\mathrm{eff}} = P_{p,\mathrm{eff}}\left[-\frac{\lambda_p\alpha_p}{\lambda_s\alpha_s} + \frac{g\Gamma}{1+\beta P_p}\frac{\lambda_p}{\lambda_s\alpha_s}\right], \tag{9b}$$

$$P_{i,\mathrm{eff}} = P_{p,\mathrm{eff}}\left[-\frac{\lambda_p\alpha_p}{\lambda_i\alpha_i} + \frac{g\Gamma}{1+\beta P_p}\frac{\lambda_p}{\lambda_i\alpha_i}\right]. \tag{9c}$$

Equations (9) elucidate that in the efficient regime any increase in the gain of the laser will directly lead to an increase in the signal and idler powers, while the pump power remains unchanged. Similar to doubly resonant IOPOs, there is an unstable SOPO operating regime at extremely high pump powers [7]. SOPOs instability at extremely high pump powers merits a separate study.

B. Numerical Example

In order to examine the three regimes of operation discussed here, we study the behavior of a type-II phase-matched BRL. The active region for the pump is a double QW of InGaAs/GaAs with emission wavelength at $\lambda_p = 980$ nm (TE polarized). A three-parameter gain relation similar to that of [23] was chosen for the 6 nm InGaAs wells. The wavelengths of the signal (TM polarized) and idler (TE polarized) are taken to be at $\lambda_s = 1550$ nm and $\lambda_i = 2665$ nm, respectively. Table 1 summarizes the waveguide geometry and parameters of interest used in simulations.

Figure 2(a) shows the calculated powers of the pump, signal, and idler as functions of current. In the figure, the circles show the simulated powers obtained from numerical solution of the rate equations in Eq. (3), whereas the solid curves show the analytically calculated values obtained from Eqs. (7)–(9). The numerical values were obtained through recording the final power values after solving the system of equations using a Runge–Kutta algorithm [24]. A close agreement between the values of both calculations is obtained.

The SOPO is fundamentally a diode laser lasing at the pump wavelength with the second order nonlinearity of the structure phase matched for nonlinear conversion within the cavity. However, the pump power-current curve deviates significantly from a conventional diode laser. The SOPO pump

Table 1. Design Parameters for the Test Structure

Parameter	Value	Parameter	Value
λ_p (nm)	980	α_σ	$\alpha_{l,\sigma}+\alpha_{m,\sigma}$
λ_s (nm)	1550	$\alpha_{m,\sigma}$	$(\ln\sqrt{R_1R2})/L$
λ_i (nm)	2665	$\alpha_{l,\sigma}$(/cm)	2.00
n_p	3.2765	$\sqrt{R_1R_2}$	0.97
n_s	3.2547	L (μm)	250
n_i	3.2163	Γ	0.032
$v_{g;p}$ (cm/s)	7.14×10^9	V_{ph} (cm^3)	1.25×10^{-10}
$v_{g;s}$ (cm/s)	8.79×10^9	β(/W)	2.0706
$v_{g;i}$ (cm/s)	9.20×10^9	$\langle\chi^{(2)}_{\text{eff}}\rangle/\sqrt{A^{(2)}_{\text{eff}}}$(/V)	80.06×10^{-6}

power has different characteristics in the three efficiency regimes as indicated on Fig. 2(a). While in the no OPO regime, the laser acts akin to a conventional diode laser, in the efficient regime that ensues at currents between 25.5 and 91.5 mA: the pump output saturates at 250.5 mW irrespective of the injected current. In this regime, the excess injected carriers translate into pump photons that are all converted into signal and idler photons. Finally, at currents above 91.5 mA, the SOPO enters the inefficient regime of operation and the pump power increases with current but with a lower slope compared to the no OPO regime. In this example, the pump slope efficiency is 9.98 W/A within the no OPO regime and 3.01 W/A within the inefficient regime. Such a reduction in the pump slope efficiency is due to the partial conversion of pump photons into signal and idler in the inefficient regime.

As illustrated in Fig. 2(a), the power of both signal and idler increases with increasing the current at regions above the OPO threshold current. The signal or idler power curve versus current can be interpreted in a similar fashion to the power-current curve in a conventional laser. While in a conventional laser, current controls the gain, in the SOPO, current indirectly affects the parametric gain of the device through changing the pump power. The signal/idler slope efficiencies in the inefficient regime are lower than those in the efficient regime. The slope efficiency is 6.39(3.37) W/A in the efficient, and 4.93(2.61) W/A in the inefficient regime for signal (idler), respectively. This change in the slope efficiencies demonstrates the reasoning behind naming both regimes. The change in the SOPO signal power slope is attributed to a change in the mode of operation due to a change in the parametric gain mechanism. This behavior is also similar to the change in the slope efficiency of a conventional diode laser due to nonlinear gain mechanisms leading to lasing of other modes in addition to the fundamental mode.

Frequency chirp is defined as $1/2\pi d\phi/dt$ and is usually divided into transient and adiabatic components. Adiabatic chirp or the steady-state chirp can be calculated from the steady-state powers and $\Delta\phi$ using Eqs. (3b), (3d), and (3f). Figure 2(b) demonstrates the dependence of the frequency chirp on injected current for the simulated SOPO. From the figure, the analytically calculated chirp is in good agreement with those obtained numerically. Note that the signal and idler chirp are not plotted in the no OPO region, where signal and idler powers are merely quantum fluctuations.

An important feature in Fig. 2(b) is the very large signal and idler adiabatic frequency chirp, which is in the order of a few

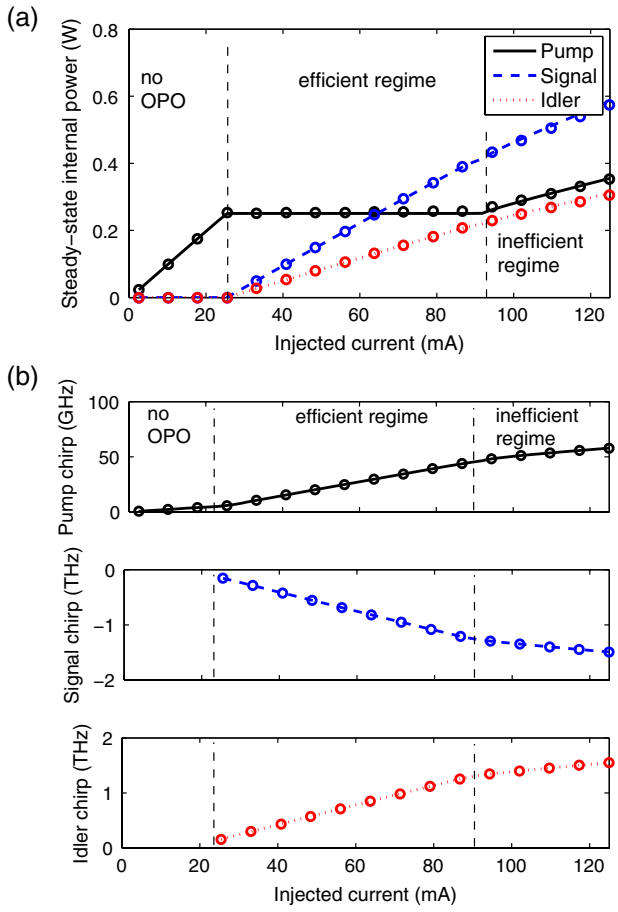

Fig. 2. (a) Steady-state internal power of the pump, signal and idler and (b) adiabatic frequency chirp of the simulated SOPO plotted as functions of the injected current. The lines and circles represent the analytically and numerically calculated data, respectively. The steady-state regions of operation are separated with vertical dashed lines and are distinct from the change in the slope of the graphs.

terahertz. This large frequency deviation can be explained through the tuning curve of the structure. Figure 3 shows the tuning curve of the BRL SOPO under study calculated through modal analysis. A small change in the pump frequency/wavelength leads to relatively large changes in the signal and idler frequencies/wavelengths. For the device studied here, a shift in the emission wavelength of the diode pump by an amount of 2 nm results in tuning of the signal wavelength between 1550–1568 nm and tuning of the idler wavelength between 2665–2627 nm. It can be shown that in the frequency chirp relations, Eqs. (3b), (3d), and (3f), the first term is usually much larger compared to the second. Therefore, the chirp properties of the device follow those of $\Delta\omega_\sigma$. However, the second terms have a significant effect on $\Delta\phi$ that appears in the power rate equations and defines the steady-state regime of operation. Due to carrier injection in the cavity, there is usually an appreciable adiabatic frequency chirp on the order of tens of gigahertz induced in semiconductor lasers [20]. In the case of SOPOs, this chirp is exhibited by the pump, which consequently translates into an even larger chirp for the signal and idler. This transfer of chirp from pump to signal and idler can be clearly seen in Fig. 2(b). It is important to note that the pump chirp frequency is projected negatively onto the signal while the pump chirp translation to

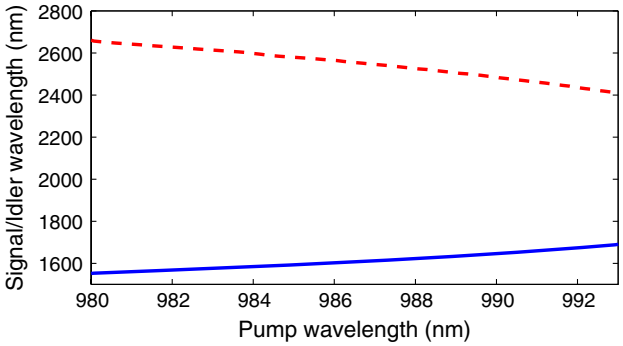

Fig. 3. Wavelength tuning curve of the simulated SOPO showing the variation of signal and idler wavelengths as functions of the pump wavelength. The figure shows that a shift in the pump wavelength by +2 nm, results in a signal and idler wavelength drift by 18 nm and −38 nm, respectively.

idler is positive. This feature and its possible applications will be discussed in more detail in the next section.

4. DYNAMIC ANALYSIS AND LARGE SIGNAL RESPONSE

The importance of investigating the SOPO large signal dynamic response is twofold: not only because it sheds light on the transient properties of SOPOs in the CW regime but it also provides insight into their response when operated in pulsed regime. To start, the time constants that represent the SOPO temporal response will be introduced. After, the rate equations are solved to examine the transient behavior of the output power and frequency.

A. Rise Time and Build-Up Time

There are two main time constants that define the response speed of SOPOs: signal/idler build-up time and rise time between 10% and 90% of the steady state value. They help determine the ultimate direct modulation speed. Build-up time is the onset for the signal and idler powers. We define the build-up time as the time needed for the input step response to rise to 10% of the steady-state value. The 10%–90% rise time is a popular metric that allows for comparing the responses of various devices. It will be referred to as the rise time. Figure 4 shows a schematic of an example transient power trace to illustrate the definition of these terms.

As opposed to numerical solutions, an analytical formula for the rise time or build-up time can provide insight into

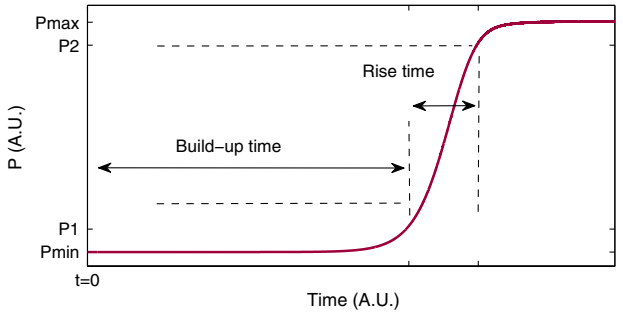

Fig. 4. Build-up time and rise time shown for a step response, assuming the turn-on time to be at $t = 0$ s. Here $P1 = P$ min $+ 0.1\Delta P$ and $P2 = P$ min $+0.9\Delta P$ where $\Delta P = P$ max $-P$ min.

the nature of the parameters affecting the response speed and it can facilitate the process of tailoring the device design for high speed modulation. A closed-form solution for the build-up time can be derived by solving the rate equations described earlier with the appropriate initial conditions. In an initially unbiased SOPO, before the build-up time the signal and idler powers are merely vacuum fluctuations, and pump depletion can be neglected. As such, the solution of Eqs. (3c) and (3e) results in exponential responses for signal and idler powers. Assuming no pump depletion, $\Delta\phi = \pi/2$, and solving for the signal and idler, a solution can be derived that relates the signal/idler power $P_{s,i}(t)$ to their initial value $P_{s,i}(0)$:

$$P_{s,i}(t) = P_{s,i}(0)\exp\left(2t\sqrt{v_{g;s}v_{g;i}\frac{\kappa^2}{\lambda_s\lambda_i}P_{p,\mathrm{fr}}}\right)\exp(-\alpha_{s,i}v_{g;s,i}t). \tag{10}$$

Here $P_{p,\mathrm{fr}}$ is the steady-state free running pump power, i.e., the pump power available to the parametric processes, which can be derived from Eq. (1a). To obtain a closed-form relation for the build-up time $\tau_{r;s,i}$, it is sufficient to define $r = 0.1P_{s,i}(\infty)/P_{s,i}(0) = P_{s,i}(\tau_{r;s,i})/P_{s,i}(0)$ and solve (10) for $\tau_{r;s,i}$:

$$\tau_{r;s,i} = \frac{\ln r}{2\sqrt{v_{g;s}v_{g;i}\frac{\kappa^2}{\lambda_s\lambda_i}P_{p,\mathrm{fr}} - \alpha_{s,i}v_{g;s,i}}}. \tag{11}$$

The constant r should be derived through quantum optical calculations to account for the quantum fluctuations that define $P_s(0)$ [25]. However, the choice of r does not strongly affect the calculation of the build-up time due to its logarithmic dependence. Moreover, although a constant $\Delta\phi$ is utilized to derive this approximation, Eq. (11) can predict the build-up time for both SOPO steady-state regimes, efficient and inefficient, as will be demonstrated.

Equation (11) predicts that the OPO build-up time can be reduced by tuning physical device parameters such as loss and nonlinear coefficient or external parameters such as the pump power available for nonlinear conversion. Tuning the structural or physical parameters are not easily achievable for a given device whereas the pump power can be tuned easily through the injected current. Although the rise times can not be expressed analytically similar to the build-up times, it can be shown numerically that the same parameters will affect their values. The effects of the initial bias and current injection step size on the build-up and rise times will be studied in the forthcoming subsections alongside other dynamic properties.

B. Dynamic Behavior for an Initial Condition of Zero Bias

In order to serve as a reference for the SOPO dynamics, the dynamic behavior of a conventional laser that is not phase matched for nonlinear conversion is provided. The structure described in Table 1 is essentially a diode laser, which is phase matched for efficient nonlinear conversion. If the second order nonlinear interactions are excluded, the device will perform as a conventional diode laser. The threshold current of this unphasematched diode laser is as low as $I_{\mathrm{th}} = 0.252$ mA owing to the device small size and high facet reflectivity. The

response of the laser assuming a zero initial current is plotted in Fig. 5 through solving Eq. (1) with a Runge–Kutta algorithm. The behavior exhibits the well-known laser relaxation oscillations. These oscillations become less pronounced as the current increases. The changes in the laser carrier density together with the relaxation oscillations induce transient chirp on the order of tens of gigahertz. This increase in the frequency shift is often called "positive" chirp and usually negatively impacts the performance of dispersive telecommunication systems that rely on direct modulation of lasers as a source.

The response of the conventional diode laser for currents in the vicinity of those typically needed to reach oscillation threshold in SOPOs is also studied to serve as a reference. The SOPO discussed above has an OPO threshold current of 25.5 mA which is about two orders of magnitude larger than the pump laser threshold value. The dynamic behavior is shown in Fig. 6, where only one overshoot rather than damped relaxation oscillations are observed due to the significant level of current injection. Moreover, the laser transient and adiabatic chirp are much larger due to the large swing in the injected carrier density.

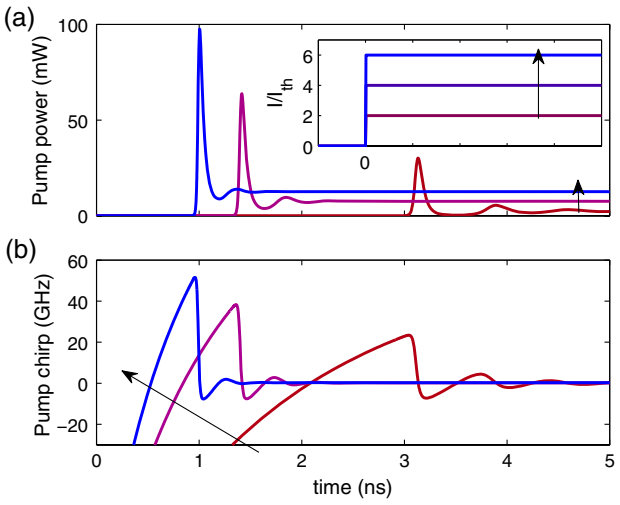

Fig. 5. (a) Pump power and (b) frequency dynamics of the un-phase-matched laser for current steps of $2I_{th}$, $4I_{th}$, and $6I_{th}$. The inset shows the injected current as a function of time.

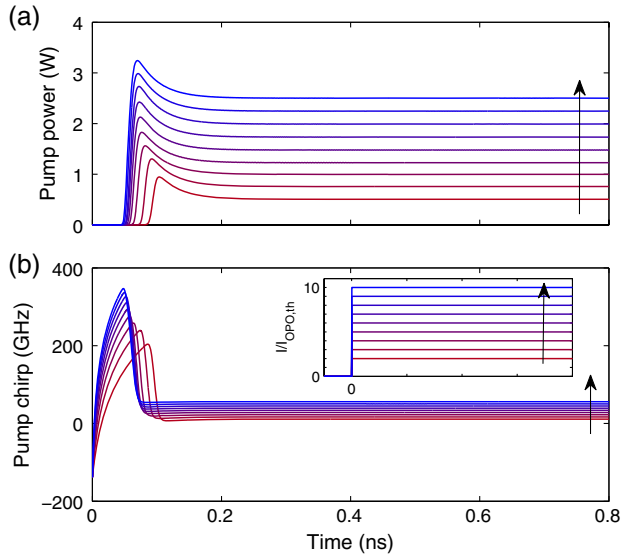

Fig. 6. (a) Power and (b) frequency dynamics of the un-phase-matched laser for currents changing from $2I_{OPO,th}$ to $10I_{OPO,th}$ in steps of $I_{OPO,th}$. The inset shows the injected current as a function of time.

1. Power Dynamics

If nonlinear conversion is taken into consideration when analyzing the example given above, the large-signal response of a phase-matched SOPO should be calculated through the solution of Eqs. (1c) and (3). The pump, signal, and idler power and chirp of the SOPO detailed in Table 1 were calculated for a current step at $t = 0$ s rising from zero to $nI_{OPO,th}$, $n = 2, 3, \ldots, 10$, where $I_{OPO,th} = 25.5$ mA as can be seen in Fig. 7. This range of bias conditions leads to the SOPO operation in efficient and inefficient regimes. By comparing the pump power dynamics in presence and lack of phase matching, it is clear that the pump behavior is altered at the onset of its conversion into the signal and idler. The onset of this change is the signal/idler build-up time at which signal and idler powers increase significantly while the pump power is depleted. Parametric gain can be seen as a power-dependent loss mechanism for the pump. Consequently, after the signal and idler buildup, the pump laser encounters not only the cavity and mirror losses but also the parametric conversion losses.

Despite the different nature of gain in a conventional diode laser and the parametric gain in an SOPO, Fig. 7 highlights the presence of relaxation oscillations in the SOPO signal/idler response akin to the un-phase-matched laser modulated near the threshold current. Comparing the signal and idler output responses of the SOPO with the output power of a conventional laser that is not phase matched unveils a notable distinction between the responses. Contrary to the case of the conventional pump laser that is not phase matched, in the SOPO there is no visible signal and idler relaxation oscillation in the vicinity of the SOPO threshold, where the signal and idler powers monotonically increase to their steady-state values. In this example, relaxation oscillations take place at currents above $3I_{OPO,th}$. The oscillation amplitude and damping time increase as the the pumping level is raised.

The current at which the SOPO shifts from the efficient to the inefficient regime of operation was found to be 95 mA for this example as can be seen in Fig. 2. Hence, the plots representing $2I_{OPO,th}$ and $3I_{OPO,th}$ in Fig. 7(a) show the operation of the device in the efficient steady-state regime. The other plots fall into the inefficient regime. It is evident that for this example the relaxation oscillations appear only in the inefficient regime. In order to investigate these fluctuations and their sources in more detail, a transient power analysis should be performed similar to those carried out in [9].

The relaxation oscillations of signal and idler are due to depletion of pump power into signal and idler to a level below the steady-state power, which leads to an undershoot in the pump power. This leads to back conversion of the parametrically generated signal and idler to increase the power to a level closer to the steady state value. This cycle may continue as a damped relaxation as can be seen in Fig. 7(a). The pronounced conversion of the parametric powers in the inefficient regime can be attributed to the intermittent change of $\Delta\phi$ whereas in the efficient regime $\Delta\phi$ does not change and has a value of $\pi/2$. Relaxation oscillations have been

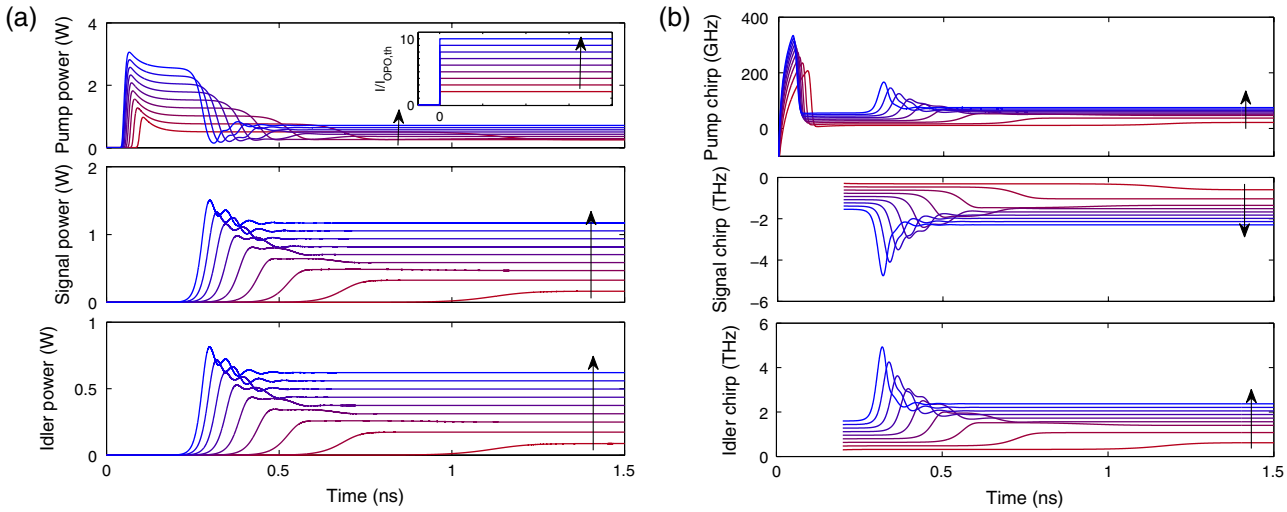

Fig. 7. (a) Power and (b) frequency dynamics of the SOPO under study for current steps of $2I_{OPO,th}$ to $10I_{OPO,th}$ in steps of $I_{OPO,th}$. The inset shows the injected current as a function of time.

shown to happen before in doubly resonant [19] and singly resonant IOPOs [9].

2. Chirp Dynamics

Frequency chirp dynamics of the SOPO are plotted in Fig. 7(b) for the same current bias conditions described in the previous subsection. To compare the SOPO/phase-matched laser with a conventional laser, Fig. 7(b) should be compared to Fig. 6(b). In the conventional un-phase-matched pump laser, the laser frequency shift reaches a steady-state value in the order of gigahertz after the laser rise time. On the other hand, for the SOPO, although the pump chirp properties behave in a similar fashion before the build-up time, pump frequency encounters additional transient chirp after the buildup of the signal and idler pulses. This effect can be attributed to depletion of the pump photons into signal and idler, which changes the pump photon density, and, consequently, varies the carrier density and, hence, the pump frequency. Moreover, additional transient chirp components can be seen in the pump frequency for currents above $3I_{OPO,th}$ due to the presence of relaxation oscillations. Relaxation oscillations alter the level of pump power as well as the carrier density leading to oscillations in the pump output wavelength.

The transient and adiabatic pump chirp characteristics get transfered to the signal and idler chirp, which reach terahertz levels for the signal and idler, compared to the gigahertz level in the pump. One of the most important features in Fig. 7(b) is the negative frequency chirp in the signal as opposed to the positive chirp that is obtained in a conventional laser. The signal frequency chirp is opposite to that of the pump and idler in its sign. Such a negative chirp can be explained through the tuning curve, which translates how the pump frequency shift influences that of the signal due to the presence of $\Delta\omega_\sigma$ terms in the model. This negative chirp could be of great benefit in chirp engineering applications in some optical communication systems.

3. Build-Up and Rise Times

The signal and idler build-up times were calculated for various currents both numerically and analytically from Eq. (11) assuming $r = 10^7$—taken after the work in [25]. Figure 8(a) shows the analytically calculated results from Eq. (11) (dotted line and triangles) and the build-up time obtained from the numerical solutions (solid line and circles). The figure demonstrates a good agreement between the analytical results and those calculated from the simulations. The signal and idler 10%–90% power rise times were calculated from the simulation data. The results are plotted in Fig. 8(b) showing rise times of tens of picoseconds. Similar to the build-up time, rise time is inversely dependent on the value of the injected current step. Moreover, it can be seen that the signal and idler rise times are nearly equal. This can be explained by the Manley–Rowe relations and the similarity of the signal and idler power ratio in a lossless OPO [26].

C. Initial Condition: Device Biased Above OPO Threshold

In order to achieve faster response time and lower transient chirp, it is common to set the initial current of diode lasers to a

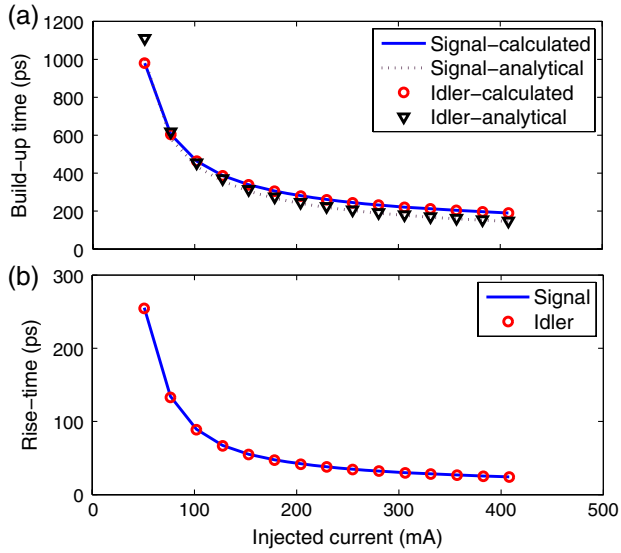

Fig. 8. Dependence of signal and idler power (a) build-up times and (b) 10%–90% rise times on injected current simulated for the example SOPO. The initial current is 0 mA.

bias point above threshold. The effect of the nonzero initial bias point on the SOPO rise and build-up times will be examined by setting the initial bias current to values above the OPO threshold. The dynamics of the reference structure described earlier were examined when the initial bias current is set to $1.1I_{\mathrm{OPO,th}}$ and $2I_{\mathrm{OPO,th}}$ in two separate cases. The response of the SOPO using step currents rising from $1.1_{\mathrm{OPO,th}}$ to $nI_{\mathrm{OPO,th}}$, $n = 2, 3, \ldots, 10$ at $t = 0$ s is plotted in Fig. 9. The output powers are assumed to be in steady state before $t = 0$ s.

Figure 9(a) shows that similar to the previous example, right after the OPO turn on; the pump power increases to a value higher than the final steady-state power (overshoot). In the case for zero initial bias current in Fig. 7(a), the pump power remains at the same level until the build-up time. In the bias condition examined here the signal and idler already have nonzero power before the turn-on time—17 and 9 mW, respectively. Consequently, depletion of pump power into the signal and idler is considerable even immediately after the device is turned on, which leads to appearance of an undershoot in the pump power right after the overshoot. A noteworthy characteristic of the pump response is the behavior of the pump power and how it reverts to the initial power level in the efficient regime (the two lowest currents) since the SOPO is driven in the efficient regime both before and after the turn-on time. Nevertheless, the signal and idler increase after the build-up time to their steady-state values with or without incurring relaxation oscillations depending on the region of operation of the SOPO, which is determined by the bias level. As discussed in the previous example, relaxation oscillations occur at current levels above $3I_{\mathrm{OPO,th}}$. The same condition is valid in this example although the oscillation magnitude and damping time are reduced owing to the reduced magnitude of the pump overshoot.

The chirp dynamics of the device for this nonzero initial current bias condition follow the same trend as what was obtained for the previous example of a zero initial bias current. As illustrated in Fig. 9(b), the first chirp overshoot in the pump frequency that takes place in the vicinity of 50 ps is drastically reduced compared to the previous example shown in Fig. 7(b). This reduction in the chirp overshoot takes place due to the smaller swing between the initial and final stages of the injected current and, hence, carrier density in this example. The second chirp overshoot, which ensues due to depletion of pump into the signal and idler, as well as the chirp oscillations thereafter due to the SOPO relaxation oscillations, are observed in this example similar to the example of zero initial bias current. However, the chirp value in this case is smaller than the corresponding chirp components in the previous example due to the reduced oscillations in the pump power. These chirp characteristics of the pump translate into the signal and idler as in earlier cases, leading to a THz level of negative and positive chirp components in the signal and idler, respectively. It is worth noting that the signal and idler chirp are plotted for the entire range of the time axis in this case as opposed to the previous case since the signal and idler powers are always nonzero.

To clearly demonstrate the effect of the initial current on the dynamic properties of the device, the response of the SOPO is plotted in Fig. 10 using step currents starting from $2I_{\mathrm{OPO,th}}$ at $t = 0$ s. It is instructive to compare this behavior with what was obtained in the previous two examples. Figure 10(a) shows that the power response of the pump, signal, and idler in this example follow the same trend as those in the $1.1I_{\mathrm{OPO,th}}$ initial current case. The pump power overshoot has decreased even further due to the higher signal and idler initial powers and, hence, the faster depletion of pump into the signal and idler. Additionally, this example confirms the inverse relation of relaxation oscillation amplitude and damping time with the initial current as explained in the previous example. Similar to the previous examples, the pump chirp components are translated negatively and positively into signal and idler, respectively, as shown in Fig. 10(b). Although there is a slight decrease in the transient chirp components of the signal and idler, these frequency components are still on the order of terahertz in value. It should be noted that despite the difference in the initial bias conditions used in the above examples, the steady-state power and chirps obtained are merely identical. This goes to demonstrate that the initial conditions of the SOPOs chiefly influence the dynamics of the response rather than the steady state.

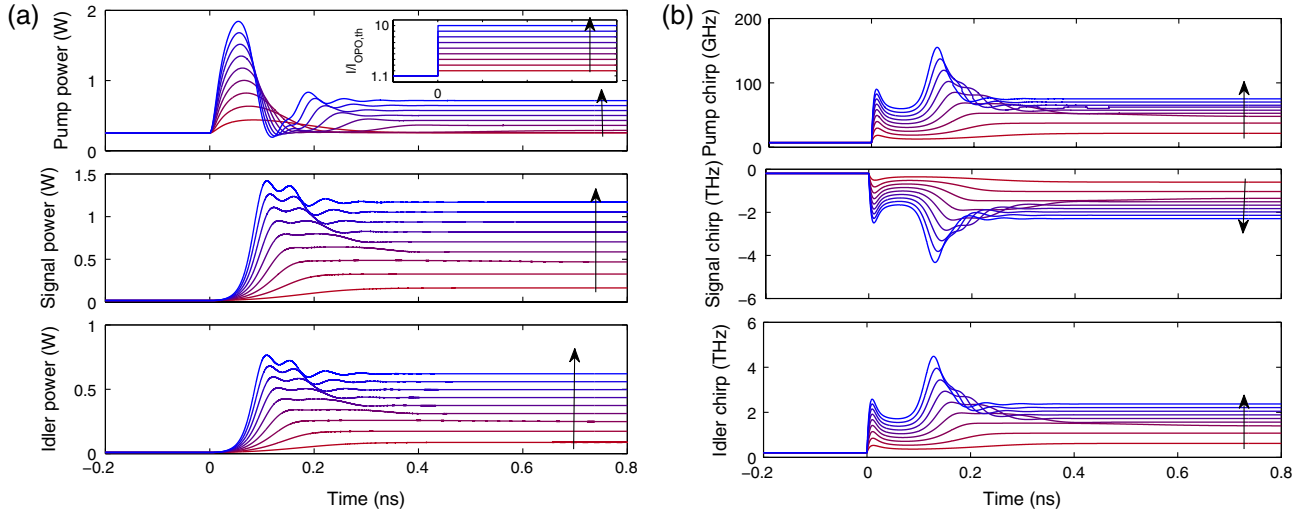

Fig. 9. (a) Power and (b) frequency dynamics of the SOPO under study for current changing from $2I_{\mathrm{OPO,th}}$ to $10I_{\mathrm{OPO,th}}$ in steps of $I_{\mathrm{OPO,th}}$. The initial current is $1.1I_{\mathrm{OPO,th}}$ as shown in the inset.

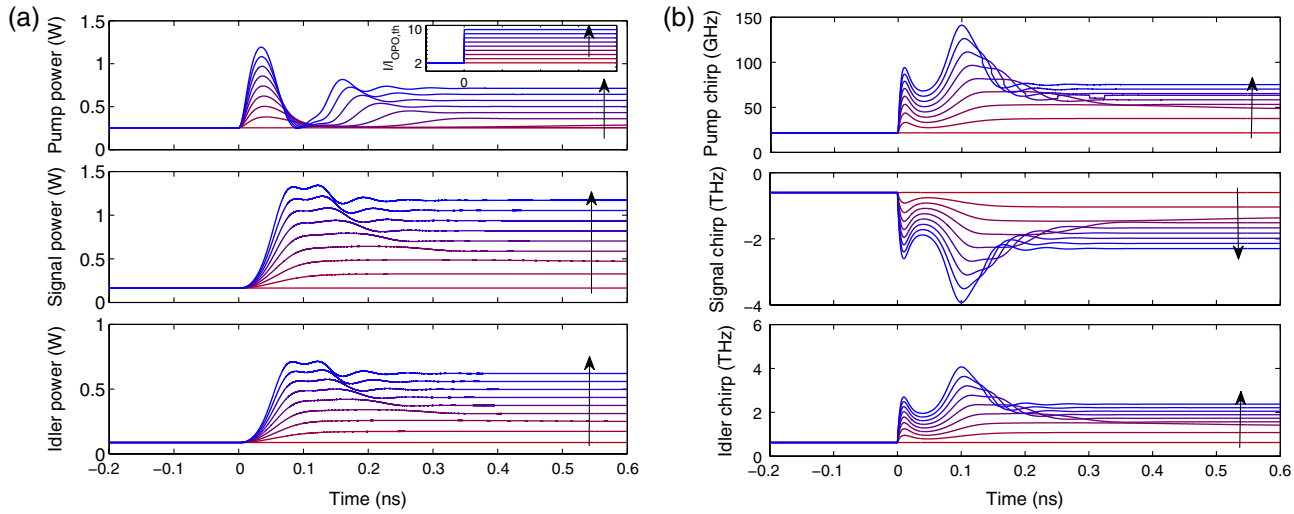

Fig. 10. (a) Power and (b) frequency dynamics of the SOPO under study for current changing from $2I_{\mathrm{OPO,th}}$ to $10I_{\mathrm{OPO,th}}$ in steps of $I_{\mathrm{OPO,th}}$. The initial current is $2I_{\mathrm{OPO,th}}$ as shown in the inset.

In the case of nonzero initial conditions, the no-pump-depletion assumption is not valid and, consequently, Eq. (11) does not hold anymore. However, the build-up time can still be calculated numerically as plotted in Fig. 11(a). The figure shows a significant decrease in the build-up time in the two examples compared to the zero initial current case. This was expected as the signal and idler have already built up in the cavity. Furthermore, the figure shows that the build-up time is inversely related to the initial bias current value.

The corresponding 10%–90% rise times are also plotted and compared to those plotted in Fig. 11(b) for both $1.1I_{\mathrm{OPO,th}}$ and $2I_{\mathrm{OPO,th}}$ currents. The figure illustrates that the rise time is reduced modestly with increasing the initial current due to the reduced time needed for the signal and idler to get to their steady-state values when starting from a nonzero power.

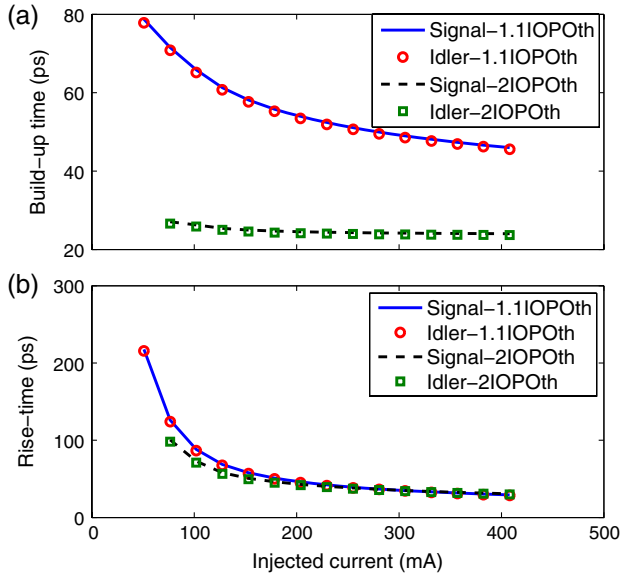

Fig. 11. Dependence of signal and idler power (a) build-up times and (b) 10%–90% rise times on injected current simulated for the example SOPO. Solid and dashed curves show the response to initial currents of $1.1I_{\mathrm{OPO,th}}$ and $2I_{\mathrm{OPO,th}}$, respectively.

The rise time converges to nearly 30 ps in all three examples studied at sufficiently high current steps. It can be concluded that while the main advantage of biasing the device above OPO threshold is to decrease the build-up time to realistic values and tuning the build-up time, tuning the initial current at values above threshold will only modestly affect the rise time depending on the region of operation. The SOPO rise time can be tuned through other parameters such as the current swing.

5. DISCUSSION

The SOPO dynamic behavior was predicted in this work through a self-consistent analysis of the diode laser pump rate equations in conjunction with the OPO rate equations. It was evident from the analysis that the build-up time is the limiting factor in the response time of these devices. The build-up time is largely determined by the values of the nonlinear gain and the propagation losses in the cavity and will likely continue to be the limiting factors even after improving these parameters significantly. In order to circumvent the build-up time limitations, the dc bias for these devices can be set to a value above the SOPO threshold akin to the strategies employed for directly modulating semiconductor lasers.

In the structure used here to study the various current injection examples, the device suffers from lower conversion efficiency and larger chirp components in the output frequency when it is operated in the inefficient regime, compared to the efficient regime of operation. However, the former regime of operation provides superior rise and build-up times. As such, operation of the SOPO at very large currents, which essentially lead to operation in the inefficient regime, provides enhanced dynamics as a modulated source. Given the nature of the gain in SOPOs they will likely require significantly higher powers for their bias in comparison to conventional un-phase-matched laser counterparts in order to obtain reasonable transient response times. However, given the SOPO tunability and diverse wavelength coverage there may exist regions of operation where they may cater to unmet needs for certain applications. The performance of this class of devices when directly driven for ASK modulation is remarkable as the slope efficiency varies widely depending on whether

the SOPO is biased in the efficient or inefficient regimes. For a given extinction ratio in the output, bias conditions can be devised to require minimum current modulation swing. Moreover, for higher modulation current steps, significant transient and adiabatic chirp values are obtained. This excessive chirp in the signal and idler can be utilized in a beneficial fashion. A bandpass filter with a suitable narrow bandwidth can be used to engineer the output extinction ratio.

Moreover, the sign of the frequency chirp obtained in the signal is of great interest for dispersion-limited optical communication links. The chirp properties of the pump laser are translated to the signal while inverting their sign and, hence, lead to negative chirp in the signal frequency. This property can be utilized for use in prechirping the signal to act as a source for extended link lengths in optical links at 1550 nm in a fashion similar to [20,21].

6. CONCLUSION

By merging the analysis tools available for diode lasers and OPOs, a set of nonlinear differential equations was developed that relate the carrier density with the pump, signal, and idler temporal characteristics in an electrically injected intracavity SOPO. It was shown that similar to the bulk doubly resonant IOPOs, SOPOs have two stable regions of operation: the efficient and inefficient regimes. The efficient regime leads to lower transient chirp and more efficient generation of signal and idler, compared to the inefficient regime of steady-state operation. However, the inefficient regime takes place at higher injection levels that offer higher output powers and faster rise times. The effect of initial conditions of the SOPO on its dynamic properties were studied to highlight the tuning ability of the build-up time through the initial conditions. The notable chirp dynamics of SOPOs, including the negative chirp exhibited by the signal, were also discussed and a possible application in optical communication systems employing ASK modulation format was proposed.

APPENDIX A

The terms $\Delta\omega_s$ and $\Delta\omega_i$ in Eqs. (3d) and (3f) represent the deviation of signal and idler angular frequencies from their values at laser threshold only due to laser frequency chirp $\Delta\omega_p$. To derive the numerical value of these terms based on $\Delta\omega_p = (\alpha/2)v_{g;p}(\Gamma g - \alpha_p)$ it is assumed that $\Delta\omega_p$ is much larger than the frequency change due to nonlinear effects—the right terms in the above-mentioned equations. From the energy and momentum conservation relations,

$$\Delta\omega_p = \Delta\omega_s + \Delta\omega_i, \tag{A1}$$

$$(\omega_p + \Delta\omega_p)(n_p + \Delta n_p) = (\omega_s + \Delta\omega_s)(n_s + \Delta n_s) + (\omega_i + \Delta\omega_i)(n_i + \Delta n_i), \tag{A2}$$

where Δn_σ are the changes in the effective index due to carrier injection in case of pump and phase-matched frequency shift for signal and idler.

By injection of carriers into the laser/SOPO cavity, the pump effective index varies, and consequently, the pump angular frequency shifts as much as $\Delta\omega_p = -\Delta n_p \omega_p v_{g;p}/c$. By neglecting the second-order changes such as $\Delta\omega_\sigma^2$ and Δn_σ^2, Eq. (A2) can be simplified to

$$\Delta\omega_p n_p + \frac{\omega_p \Delta\omega_p}{-\omega_p v_{g;s}/c} = \Delta\omega_s n_s + \omega_s \Delta n_s + \Delta\omega_i n_i + \omega_i \Delta n_i. \tag{A3}$$

The group index at signal/idler is defined as $n_{g;s,i} = n_{s,i} + \omega_{s,i}(\Delta n_{s,i}/\Delta\omega_{s,i})$. If this expression is substituted in the above, $\Delta\omega_s$ can be derived as reported in Eq. (5b).

Lastly, note that $\Delta\omega_\sigma$ terms were derived by utilizing the energy conservation condition—Eq. (12). Hence, $\Delta\omega_p - \Delta\omega_s - \Delta\omega_i = 0$ and $d\Delta\phi/dt$ does not include the $\Delta\omega_t$ terms as shown below:

$$\frac{d\Delta\phi}{dt} = -\kappa\frac{K}{2}\left[\frac{v_{g;p}}{\lambda_p}\sqrt{\frac{P_s P_i}{P_p}} - \frac{v_{g;s}}{\lambda_s}\sqrt{\frac{P_p P_i}{P_s}} - \frac{v_{g;i}}{\lambda_i}\sqrt{\frac{P_s P_p}{P_i}}\right] \times \cos(\Delta\phi)\mathrm{sinc}(\Delta kL). \tag{A4}$$

This property has a major effect in the steady-state power and regimes of operation of SOPOs as outlined in Section 3.

REFERENCES

1. G. M. Gibson, M. Ebrahimzadeh, M. J. Padgett, and M. H. Dunn, "Continuous-wave optical parametric oscillator based on periodically poled KTiOPO4 and its application to spectroscopy," Opt. Lett. **24**, 397–399 (1999).
2. D. Brüggemann, J. Hertzberg, B. Wies, Y. Waschke, R. Noll, K.-F. Knoche, and G. Herziger, "Test of an optical parametric oscillator (OPO) as a compact and fast tunable Stokes source in coherent anti-Stokes Raman spectroscopy (CARS)," Appl. Phys. B **55**, 378–380 (1992).
3. T. Henningsen, M. Garbuny, and R. L. Byer, "Remote detection of CO by parametric tunable laser," Appl. Phys. Lett. **24**, 242–244 (1974).
4. A. Ngai, S. Persijn, I. Lindsay, A. Kosterev, P. Gro, C. Lee, S. Cristescu, F. Tittel, K.-J. Boller, and F. Harren, "Continuous wave optical parametric oscillator for quartz-enhanced photoacoustic trace gas sensing," Appl. Phys. B **89**, 123–128 (2007).
5. J. Gao, F. Cui, C. Xue, C. Xie, and P. Kunchi, "Generation and application of twin beams from an optical parametric oscillator including an α-cut KTP crystal," Opt. Lett. **23**, 870–872 (1998).
6. A. Gatti, E. Brambilla, L. A. Lugiato, and M. I. Kolobov, "Quantum entangled images," Phys. Rev. Lett. **83**, 1763–1766 (1999).
7. M. Oshman and S. Harris, "Theory of optical parametric oscillation internal to the laser cavity," IEEE J. Quantum Electron. **4**, 491–502 (1968).
8. V. I. Emel'yanov, "Phase fluctuations in a parametric light source operating inside a laser resonator," Sov. J. Quantum Electron. **2**, 524 (1973).
9. G. Turnbull, M. Dunn, and M. Ebrahimzadeh, "Continuous-wave, intracavity optical parametric oscillators: an analysis of power characteristics," Appl. Phys. B **66**, 701–710 (1998).
10. T. Debuisschert, J. Raffy, J.-P. Pocholle, and M. Papuchon, "Intracavity optical parametric oscillator: study of the dynamics in pulsed regime," J. Opt. Soc. Am. B **13**, 1569–1587 (1996).
11. Y. Yashkir and H. M. van Driel, "Passively *Q*-switched 1.57 um intracavity optical parametric oscillator," Appl. Opt. **38**, 2554–2559 (1999).
12. D. J. M. Stothard and M. H. Dunn, "Relaxation oscillation suppression in continuous-wave intracavity optical parametric oscillators," Opt. Express **18**, 1336–1348 (2010).
13. J. B. Khurgin, E. Rosencher, and Y. J. Ding, "Analysis of all-semiconductor intracavity optical parametric oscillators," J. Opt. Soc. Am. B **15**, 1726–1730 (1998).
14. Y. Ding, J. Khurgin, and S.-J. Lee, "Transversely-pumped counter-propagating optical parametric oscillators and amplifiers: conversion efficiencies and tuning ranges," IEEE J. Quantum Electron. **31**, 1648–1658 (1995).

15. P. Abolghasem and A. Helmy, "Matching layers in Bragg reflection waveguides for enhanced nonlinear interaction," IEEE J. Quantum Electron. **45**, 646–653 (2009).
16. B. J. Bijlani and A. S. Helmy, "Bragg reflection waveguide diode lasers," Opt. Lett. **34**, 3734–3736 (2009).
17. B. J. Bijlani, P. Abolghasem, and A. S. Helmy, "Intracavity parametric fluorescence in diode lasers," in *CLEO:2011—Laser Applications to Photonic Applications* (OSA/IEEE, 2011), p. PDPA3.
18. B. J. Bijlani and A. S. Helmy, "Design methodology for efficient frequency conversion in Bragg reflection lasers," J. Opt. Soc. Am. B **29**, 2484–2492 (2012).
19. R. G. Smith and J. V. Parker, "Experimental observation of and comments on optical parametric oscillation internal to the laser cavity," J. Appl. Phys. **41**, 3401–3408 (1970).
20. J. Cartledge, "Improved transmission performance resulting from the reduced chirp of a semiconductor laser coupled to an external high-Q resonator," J. Lightwave Technol. **8**, 716–721 (1990).
21. T. Saito, N. Henmi, S. Fujita, M. Yamaguchi, and M. Shikada, "Prechirp technique for dispersion compensation for a high-speed long-span transmission," IEEE Photon. Technol. Lett. **3**, 74–76 (1991).
22. G. P. Agrawal and N. K. Dutta, *Semiconductor Lasers* (Kluwer Academic, 1993).
23. S. W. C. Larry, A. Coldren, and M. L. Mashanovitch, *Diode Lasers and Photonic Integrated Circuits* (Wiley, 2012).
24. J. R. Dormand and P. J. Prince, "A family of embedded Runge–Kutta formulae," J. Comput. Appl. Math. **6**, 19–26 (1980).
25. J. Pearson, U. Ganiel, and A. Yariv, "Rise time of pulsed parametric oscillators," IEEE J. Quantum Electron. **8**, 433–440 (1972).
26. D. C. Paul and N. Butcher, *The Elements of Nonlinear Optics* (Cambridge University, 1991).